Effective detection of acetone by ZnFe$_2$O$_4$ microspheres decorated with g-C$_3$N$_4$ nanosheets

Wei Wang [a,1], Nan Zhang [b,1], Qilin Wang [a], Xin Li [a], Feng Li [c,*], Shengping Ruan [a,*]

[a] State Key Laboratory on Integrated Optoelectronics and College of Electronic Science & Engineering, Jilin University, Changchun 130012, PR China
[b] State Key Laboratory of Applied Optics, Changchun Institute of Optics, Fine Mechanics and Physics, Chinese Academy of Sciences, Changchun 130033, PR China
[c] School of Microelectronics, Northwestern Polytechnical University, Xi'an 710072, PR China

ARTICLE INFO

ABSTRACT

A single SMO limits the adsorption of gas, resulting in poor performance of the gas sensor. Herein, two-dimensional (2D) graphitic carbon nitride (g-C$_3$N$_4$) were modified on ZnFe$_2$O$_4$ microspheres as efficient gas sensing materials via hydrothermal route. The modification of g-C$_3$N$_4$ can alter the energy band structure of ZnFe$_2$O$_4$, resulting in an increase in the bandgap, thus, effectively optimizing the carrier concentration in ZnFe$_2$O$_4$ and elevating the baseline resistance of ZnFe$_2$O$_4$/g-C$_3$N$_4$ microspheres. The sensor based on ZnFe$_2$O$_4$/g-C$_3$N$_4$-20 microspheres (mass ratio of ZnFe$_2$O$_4$: g-C$_3$N$_4$ =10:2) had a higher response value (53.3) which was 3.4 times higher than that of ZnFe$_2$O$_4$, better selectivity and rapid response/recovery speeds towards 100 ppm acetone, as well as a low detection limit of 255 ppb. The enhanced performance of ZnFe$_2$O$_4$/g-C$_3$N$_4$ microsphere could be ascribed to the catalysis of C$_3$N$_4$, regulating the energy structure, and heterojunction formation between ZnFe$_2$O$_4$ and g-C$_3$N$_4$. Thus, this work demonstrated their promising applications in various fields.

1. Introduction

Acetone is a colorless volatile organic compound. As a commonly used reagent, it is widely used in semiconductor and chemical fields. However, inhaling 300–500 ppm of acetone for 5 min may cause irritation [1]. And prolonged exposure to acetone can cause headache, muscle weakness, nausea, and other symptoms. Meanwhile, acetone can be used as a biomarker in the field of medical testing [2,3]. The acetone concentration exhaled by diabetic patients usually exceeds 1.8 ppm, while that for healthy people should be lower than 0.9 ppm [4,5]. Therefore, it is necessary to detect acetone with sensitivity, selectivity and low limit of detection for protecting people's health and safety.

In recent years, the nanomaterials based on semiconducting metal oxide (SMO) have made significant progress in gas-detecting field due to their low cost, easy synthesis, high responsiveness, and fast response speed [6,7], and they show great potential in detecting various gas. It has been previously reported that a variety of SMO-based nanomaterials are promising candidates for acetone detection [8–10]. For example, Zhang et al. used ZIF-67 (zeolite imidazolate framework-67) to synthesize hollow nanocages, which showed a high response to acetone [11]. However, the sensing performance of acetone needs to be improved, especially in terms of selectivity and operating temperature. Therefore, different strategies can be used to improve the gas sensitivity of SMO, including pore formation [12], heterostructure construction [13], and catalyst loading [14].

Among them, the surface modification is the most widely accepted method to improve the gas sensing ability of SMOs. The effect of surface modification is usually expressed as electron sensitization, which originates from the flow of carriers between the host material and the modified material. According to the recent research on n-SnO$_2$ nanowires functionalized with n-WO$_3$ nanoparticles, it was found that the modulation of electron conduction channel has a significant impact on gas-sensing performance, suggesting that inhibition of nanowires conduction channel can enable selective detection of reducing gases [15]. In addition, the surface modification can change the electronic energy band structure of the material and cause the band gap to change, thereby effectively optimizing the carrier concentration in the host material and regulating the baseline resistance of the sensor.

More recently, as a kind of spinel-type binary metal oxide, zinc ferrite (ZnFe$_2$O$_4$) has received great interest due to its outstanding properties in solar cells [16], Li-ion batteries [17], water splitting [18], gas sensing [19], biosensing and so on. ZnFe$_2$O$_4$ possessing a relatively

narrow bandgap of 1.9 eV is a good candidate for environmental detection [20]. However, the single-component materials have the disadvantage of rapid charge recombination and limited oxygen adsorption. To enhance gas sensing properties, more and more concerns have focused on the hybrid heterojunctions constructed by different semiconductors with well-matched band alignments [21]. For instance, Qu et al. prepared porous mixed $Co_3O_4/NiMoO_4$ core-shell nanowires for high-performance xylene detection [22].

Recently, a metal-free two-dimensional (2D) π-conjugated polymer, g-C_3N_4 has become a research hotspot due to its flexible structure, rich defect, visible-light adsorption ability, ease of synthesis, and low economic cost [23,24]. It has a suitable band gap of 2.7 eV as a gas-sensing material [25,26], and its lamellar structure is conducive to gas adsorption. However, the gas sensing performance of g-C_3N_4 is limited because of its high carrier recombination rate and low specific surface area. Fortunately, due to the well-crystallized lamellar structure, g-C_3N_4 can easily anchor and coat on the surface of other base materials to form heterojunctions, which were proven to be effective in gas detection [27].

In the present work, the hetero-structural nanomaterial ($ZnFe_2O_4$/g-C_3N_4) made by coupling the $ZnFe_2O_4$ microsphere with different amounts of g-C_3N_4 was reported. A series of characterization results showed that the surface of $ZnFe_2O_4$ microspheres was successfully decorated with g-C_3N_4 nanosheets. The gas-sensing tests for pure $ZnFe_2O_4$ and the composites were performed and discussed in detail. The results showed that compared with pure $ZnFe_2O_4$ microspheres, the acetone sensing ability of $ZnFe_2O_4$/g-C_3N_4 microspheres was significantly improved. Moreover, a detailed possible mechanism for acetone sensitivity over $ZnFe_2O_4$/g-C_3N_4 composite was proposed.

2. Material and methods

2.1. Materials

Ferric nitrate ($Fe(NO_3)_2 \cdot 9\ H_2O$), zinc nitrate (($ZnNO_3)_2 \cdot 6\ H_2O$) and melamine were provided by Beijing Chemicals Co., Ltd. Glycerol and isopropanol were obtained from Tianjin Fuyu Fine chemical Co., Ltd.

2.2. Synthesis of g-C_3N_4

The bulk g-C_3N_4 powder was prepared by thermal condensation of melamine. The specific synthesis included a two-step continuous calcination process. First, a certain amount of melamine was heated to 500 °C for 2 h at 10 °C/min. Then, it was heated to 520 °C with a rate of 2 °C/min and maintained for another 2 h. The resulting yellow product was collected and ground into fine powder for further use.

2.3. Preparation of $ZnFe_2O_4$/g-C_3N_4 nanocomposites

Firstly, 0.076 g $Fe(NO_3)_2 \cdot 9\ H_2O$ and 0.028 g ($ZnNO_3)_2 \cdot 6\ H_2O$ were dissolved into a colorless solution contained 30 ml of isopropanol and 6 ml of glycerol under vigorous stirring. After 20 min, the obtained g-C_3N_4 with different amounts (10, 20, 30 and 40 wt%) were added into it. The suspension was then hydrothermally treated at 180 °C for 6 h in a reaction kettle with a volume of 40 ml. The precipitate was obtained by centrifugation and drying. Finally, $ZnFe_2O_4$/g-C_3N_4 nanocomposites were synthesized by annealing the precursor in air with the condition of 400 °C and 2 h. The four samples are named $ZnFe_2O_4$-10, $ZnFe_2O_4$-20, $ZnFe_2O_4$-30 and $ZnFe_2O_4$-40, respectively, for convenience.

2.4. Characterization

The X-ray diffraction (XRD) test was carried out in the range of 10–80° using Cu Kα radiation (λ = 1.5418 Å; Rigaku TTR-III). The morphology images were obtained using a scanning electron microscope (SEM; JEOL JSM-7500 F) with an acceleration voltage of 5 kV. TEM (transmission electron microscope) images, the energy dispersive spectroscopy (EDS) and elemental mappings were characterized using JEOL JEM-3010. UV-1700 spectrophotometer was used to obtain the UV–vis spectra of the samples. Photoluminescence (PL) spectra were tested using F-4600 florescence spectrophotometer (Xe lamp; excitation at 325 nm). Fourier transform infrared spectra (FTIR) were recorded on a FTIR absorption spectrometer (Thermo Scientific iS50 ATR). X-Ray photoelectron spectroscopy (XPS) was tested using VG ESCALAB MK II spectrometer (Mg Kα; 1253.6 eV).

2.5. Manufacturing and testing of the sensors

First, the prepared powder of $ZnFe_2O_4$ or $ZnFe_2O_4$/g-C_3N_4 was mixed with deionized water at 1:4 by weight and ground into a uniform slurry. The paste was then evenly coated on the surface of a hollow ceramic tube with a pair of Au electrodes and Pt leads. The four Pt leads of the ceramic tube were welded to a hexapod socket, and a Ni-Cr heating wire was welded to the center of the tube to supply operating temperature.

The resistance change of the device was monitored by an intelligent gas-sensing analyzer (CGS-8; Elite Technology, Beijing) under atmospheric condition (25 °C, ~30 RH%). For the devices based on n-type materials, the response value (S) is calculated by R_a/R_g, where R_a and R_g are the resistances of the device in air and the detected gas, respectively. The response/recovery time is the time elapsed from the initial point of the resistance change to 90% of the total change.

3. Results and discussion

3.1. Characterization

Fig. 1a shows the XRD patterns of g-C_3N_4, $ZnFe_2O_4$ and $ZnFe_2O_4$/g-C_3N_4 composites. The peaks of pure $ZnFe_2O_4$ at 2θ = 29.9, 35.3, 42.8, 56.6 and 62.2° were indexed to the (220), (311), (400), (511) and (440) of the franklinite structured $ZnFe_2O_4$ phase (JCPDS 22–1012) [28]. For the pure g-C_3N_4, the two characteristic peaks at 27.42° and 13.08° can be indexed as (0 0 2) and (1 0 0) planes [29,30]. For the $ZnFe_2O_4$/g-C_3N_4 composites materials, the feature peaks of both g-C_3N_4 and $ZnFe_2O_4$ phases were detectable. The intensity of the peak indexed to (0 0 2) plane of g-C_3N_4 in the composites gradually increased with the increase of g-C_3N_4 content. Moreover, there is no diffraction peak of other crystal impurities.

The light absorption properties of g-C_3N_4, $ZnFe_2O_4$, and $ZnFe_2O_4$/g-C_3N_4 hybrids were measured by UV–vis DRS, as shown in Fig. 1b. It was clearly seen that all the as-prepared nanomaterials showed fundamental absorption in visible light region. Compared with pristine g-C_3N_4, the band edge of $ZnFe_2O_4$/g-C_3N_4 showed redshift. The observed redshift in the composite may be attributed to their interfacial interaction [31]. The band gap (E_g) of the samples can be calculated [32], and the results are shown in the inset of Fig. 1b. The estimated direct band-gap values are 1.90, 2.08, 2.19, 2.41, 2.62 and 2.70 eV, which correspond to sample $ZnFe_2O_4$, $ZnFe_2O_4$-10, $ZnFe_2O_4$-20, $ZnFe_2O_4$-30, $ZnFe_2O_4$-40 and pure g-C_3N_4. Thus, it can be concluded the g-C_3N_4 modification will increase the band gap in $ZnFe_2O_4$/g-C_3N_4 samples.

Fig. 1c showed the FT-IR spectra of the $ZnFe_2O_4$, g-C_3N_4, and $ZnFe_2O_4$/g-C_3N_4 composites in 4000–500 cm^{-1} region. There is a peak located at 806 cm^{-1}, which results from characteristic breathing triazine units. And the peaks in the range of 1246–1634 cm^{-1} are derived from bridging C-NH-C units or trigonal C-N(-C)-C (full condensation) [33]. Additionally, the peak at 571 cm^{-1} appeared in the samples containing $ZnFe_2O_4$, which was assigned to the tetrahedral FeO_6 groups of spinel-type compounds.

As shown in Fig. 1d, the PL measurements of $ZnFe_2O_4$, g-C_3N_4 and $ZnFe_2O_4$/g-C_3N_4 composites were carried out with the excitation wavelength of 325 nm to study the properties of photo-excited charge carriers [34]. It is clearly seen that, the $ZnFe_2O_4$, g-C_3N_4 and $ZnFe_2O_4$/g-C_3N_4 had strong emission peaks centered at about 460 nm, resulting from the recombination of carriers. And the intensity of PL for
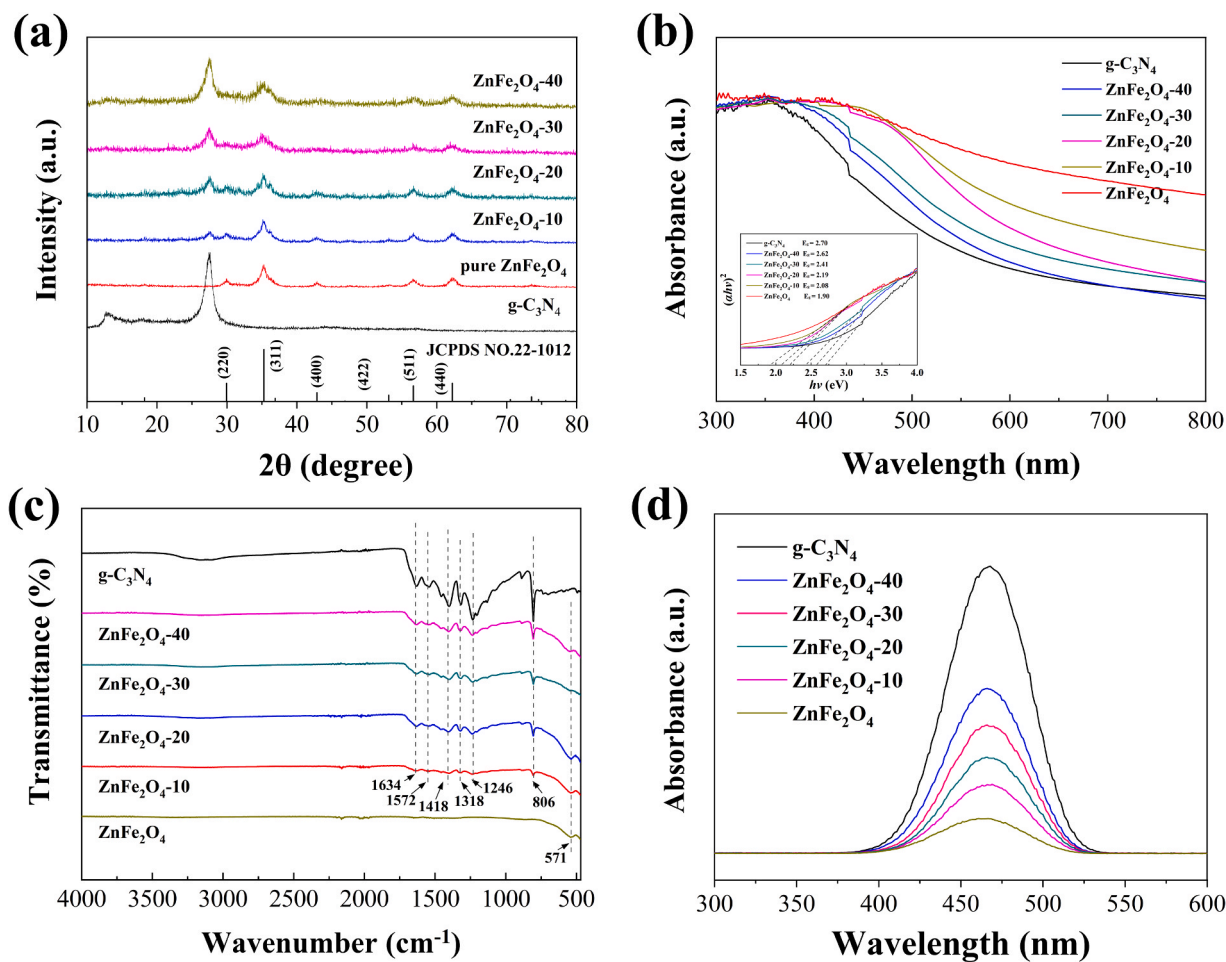
Fig. 1. (a) Powder X-ray diffraction patterns; (b) UV–vis diffuse reflectance spectra; (c) Fourier transform infrared (FTIR) spectra in the range of 4000 - 500 cm^{-1}; (d) room-temperature photoluminescence (PL) spectra (λ_{ex} = 325 nm) of g-C_3N_4, $ZnFe_2O_4$ and $ZnFe_2O_4$/g-C_3N_4 samples.
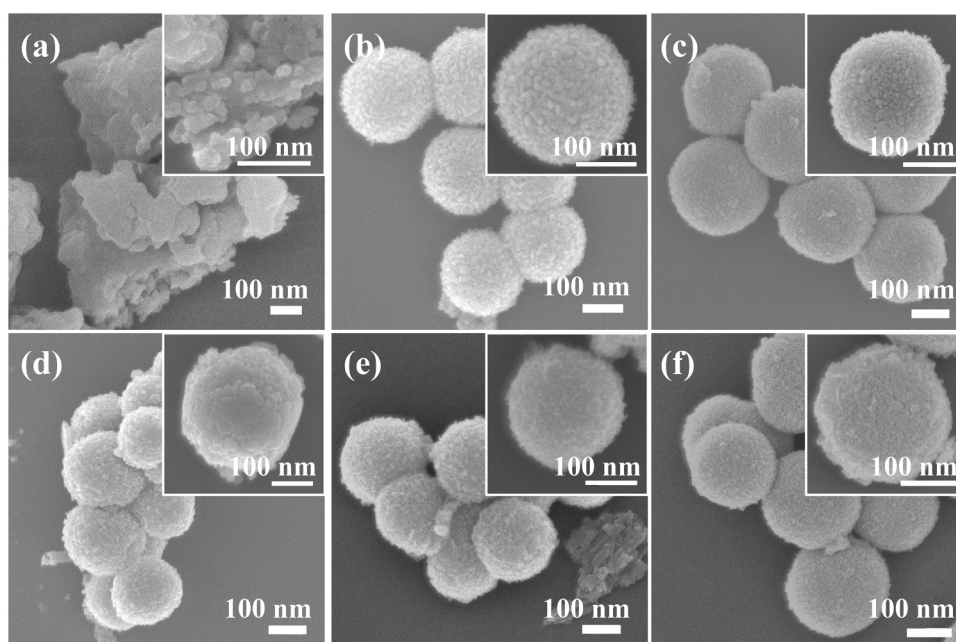

Fig. 2. Typical SEM images of (a) pure g-C_3N_4; (b) pristine $ZnFe_2O_4$ microsphere; (c) $ZnFe_2O_4$-10; (d) $ZnFe_2O_4$-20; (e) $ZnFe_2O_4$-30; (f) $ZnFe_2O_4$-40.

the composites decreased significantly with the introduction of g-C$_3$N$_4$, which is attributed to the transfer of excited electrons between the g-C$_3$N$_4$ and ZnFe$_2$O$_4$, indicating the formation of heterojunction [35]. It was clearly observed that ZnFe$_2$O$_4$-20 and ZnFe$_2$O$_4$-30 samples had the lower peak intensity compared with other samples due to the low recombination rate of the photo-generated carriers.

The SEM and TEM were employed to investigate the microstructures of the g-C$_3$N$_4$, ZnFe$_2$O$_4$, and ZnFe$_2$O$_4$/g-C$_3$N$_4$ samples (Fig. 2 and Fig. 3). It can be found in Fig. 2a that the g-C$_3$N$_4$ showed a morphology of several crumpled graphene-like stacking layers. As shown in Fig. 2b–f, ZnFe$_2$O$_4$ and ZnFe$_2$O$_4$-10, 20, 30, 40 samples possessed the spherical nanostructure with an approximate diameter of 250–350 nm. The rough surface of the samples implied that these microspheres were built from

plenty of original nanoparticles, and hence they can effectively enhance the gas sensing performance [36]. Fig. 3a and b exhibited the interior structures of pure ZnFe$_2$O$_4$ and ZnFe$_2$O$_4$-20 microsphere by TEM analysis, respectively. The dark edges and relatively bright center in Fig. 3a demonstrated the hollow structure of pure ZnFe$_2$O$_4$. It can be seen in Fig. 3b, the ZnFe$_2$O$_4$ hollow spheres turned into solid structures after introducing g-C$_3$N$_4$. And the lattice fringes in the high-resolution TEM (HRTEM) were 0.320 nm and 0.254 nm (Fig. 3c), corresponding to the (002) plane of g-C$_3$N$_4$ and (311) plane of ZnFe$_2$O$_4$, respectively. In addition, the corresponding EDS mapping images for a representative ZnFe$_2$O$_4$/g-C$_3$N$_4$ microsphere were illustrated in Fig. 3d–i, from which one could clearly see that the elements Zn, Fe, N, C, and O distribute homogeneously and uniformly. As shown in Fig. 3j, the EDS elemental

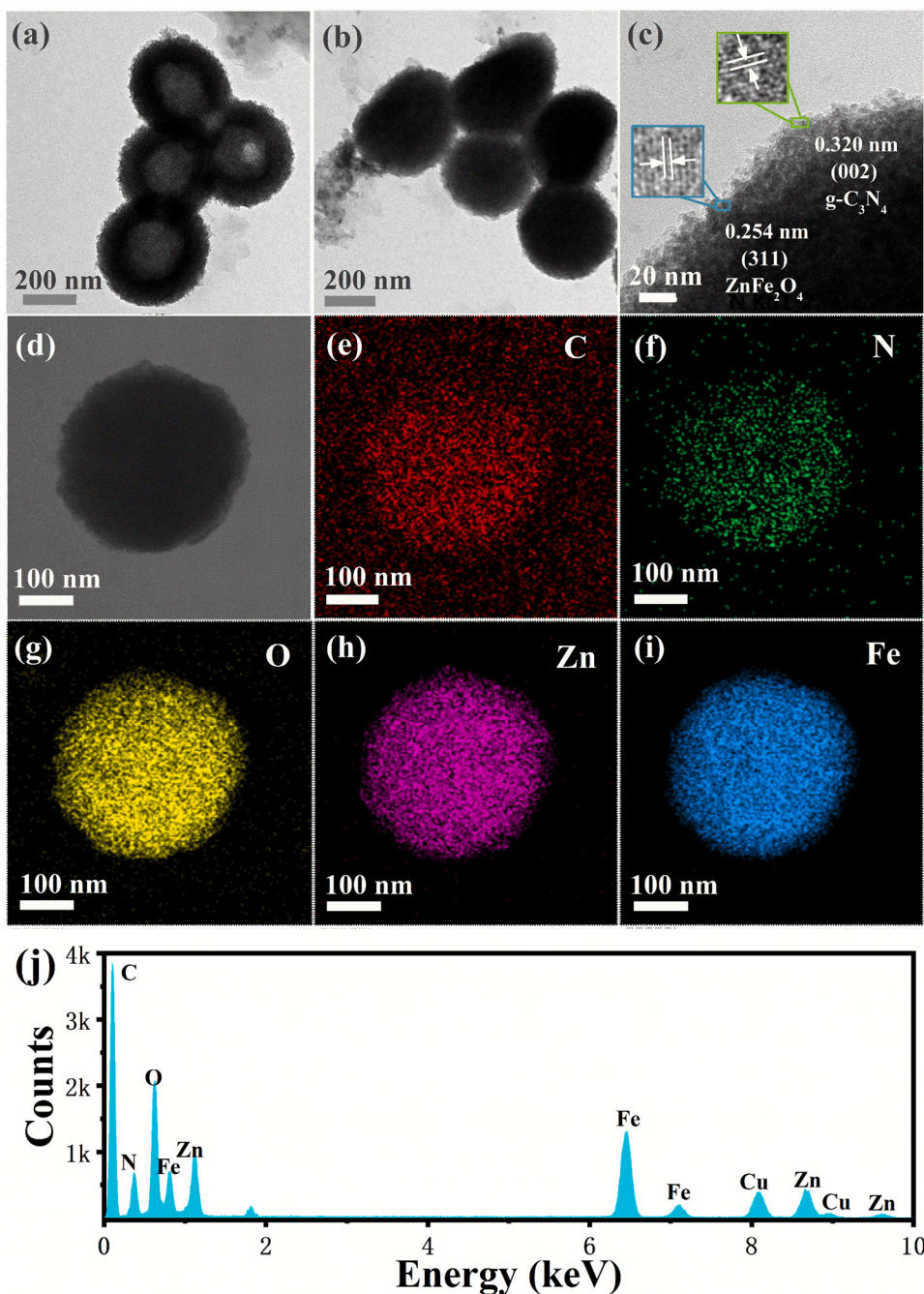**Fig. 3.** (a) and (b) TEM images of hollow ZnFe$_2$O$_4$ microsphere and ZnFe$_2$O$_4$-20 microsphere; (c) HRTEM image taken from (b); (d) Scanning TEM image of ZnFe$_2$O$_4$-20; (e)-(i) The elemental mapping extracted from STEM-EDX showing the distribution of the compositional elements (C, N, O, Zn and Fe); (j) Spots pattern of ZnFe$_2$O$_4$-20 microspheres.
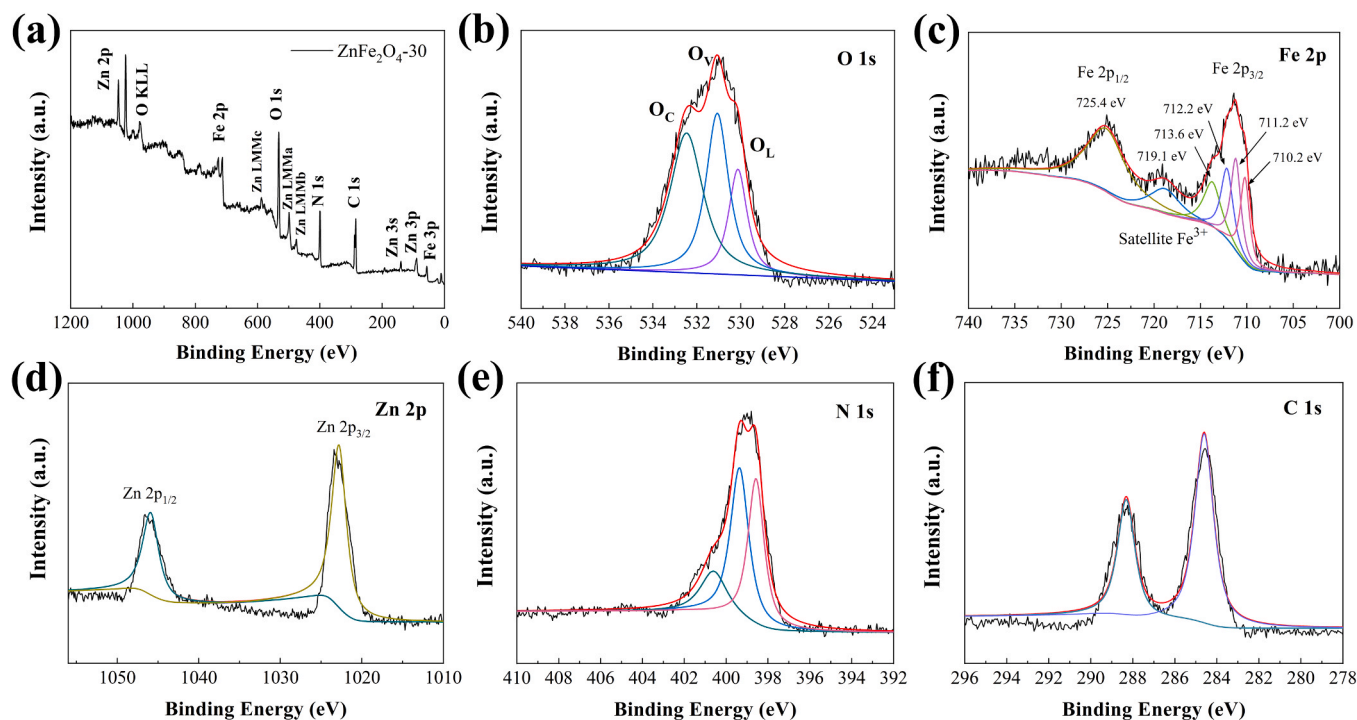
Fig. 4. (a) X-ray photoelectron survey spectra and the corresponding high-resolution XPS spectra: (b) O 1 s; (c) Fe 2p; (d) Zn 2p; (e) N 1 s; (f) C 1 s of ZnFe$_2$O$_4$–20 sample.
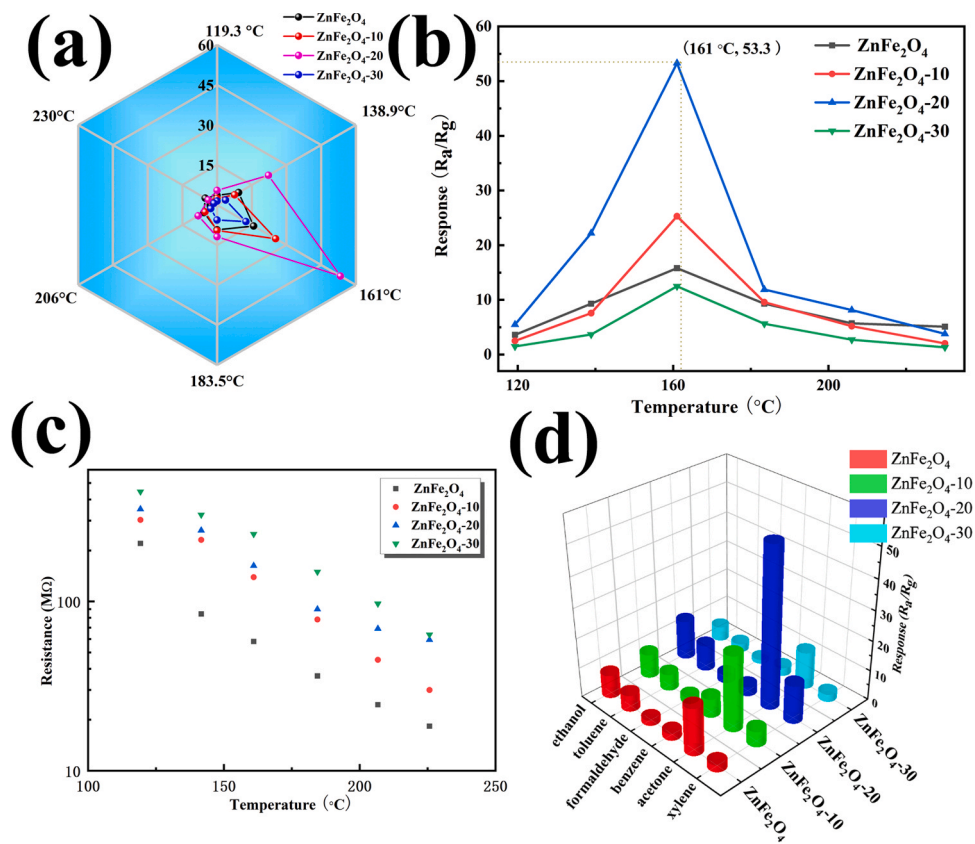
Fig. 5. (a) Radar graph and gas responses (R$_a$/R$_g$) of pure ZnFe$_2$O$_4$, ZnFe$_2$O$_4$-10, ZnFe$_2$O$_4$-20, and ZnFe$_2$O$_4$-30 to 100 ppm acetone at 119.3 − 230 °C; (b) responses of the sensors to 100 ppm of acetone at 119.3–230 °C; (c) the baseline resistance of the sensors versus different operating temperature; (d) responses of the four sensors to 100 ppm various gases at 161 °C.

spectrum showed that the $ZnFe_2O_4$-20 sample was mainly composed of Fe, Zn, C, O, and N elements in the composites.

To study the elemental composition, the XPS test was performed (Fig. 4). Fig. 4a shows the XPS spectrum of the $ZnFe_2O_4$-20 composite, indicating the coexistence of N, C, O, Fe, and Zn elements. The surface state of oxygen has an important impact on the sensing behavior of semiconductors. It can be seen from Fig. 4b that the high-resolution spectrum of O 1 s can be well fitted into three characteristic spectral lines, corresponding to the surface lattice oxygen (O_L, 530.1 eV), oxygen vacancies (O_V, 531.1 eV) and chemisorbed oxygen (O_C, 532.5 eV) of $ZnFe_2O_4$ [37]. It is obvious that the surface of the composite has a high ratio of O_V and O_C, which is beneficial for the surface sensing reaction [38]. As shown in Fig. 4c, the two main peaks of Fe 2p spectra were centered at 711.3 eV and 725.4 eV, which are attributed to the states of Fe $2p_{3/2}$ and Fe $2p_{1/2}$ in $ZnFe_2O_4$ [39]. Fig. 4d shows that the signal peak of Zn $2p_{3/2}$ and Zn $2p_{1/2}$ in the Zn element located at 1022.8 and 1045.9 eV, respectively [40]. The N 1 s spectrum are divided into three peaks at 400.6 eV, 398.5 eV, and 399.3 eV, which can be assigned to C-N-H group, the C=N-C and sp^3 hybridized nitrogen atoms ($N-(C)_3$), respectively [41]. In C 1 s spectrum (Fig. 4f), two distinct peaks were located at 284.6 eV and 288.3 eV, corresponding to sp^2-hybridized carbon and the carbon bonded with $N = C-N_2$ [42]. Thus, the XPS results further confirmed the construction of $ZnFe_2O_4/g-C_3N_4$ composites.

3.2. Gas-sensing properties

In order to explore the effect of C_3N_4 modification on the gas sensitivity of $ZnFe_2O_4$, we tested the sensing performance of $ZnFe_2O_4$-10, $ZnFe_2O_4$-20, and $ZnFe_2O_4$-30 with pure $ZnFe_2O_4$ as a reference.

The surface reaction and gas adsorption process of SMOs are highly dependent on temperature. Therefore, we first measured the response of the samples to acetone at different working temperatures to determine the optimal working temperature. The radar chart in Fig. 5a shows the response of $ZnFe_2O_4$, $ZnFe_2O_4$-10, $ZnFe_2O_4$-20, and $ZnFe_2O_4$-30 in the temperature range of 119.3–230 °C. Pure $ZnFe_2O_4$ microspheres-based sensor has a mediocre response to 100 ppm acetone (R_a/R_g=15.6). However, the response performance of $ZnFe_2O_4$ microspheres modified with g-C_3N_4 is obviously improved. Compared with pure $ZnFe_2O_4$, $ZnFe_2O_4$-20 sample shows a higher response to acetone at 161 °C, with a 3.4-fold increase in response value (R_a/R_g=53.3), clearly confirming that the modification of C_3N_4 can significantly enhance the response of the sensors to acetone. However, the further increase of g-C_3N_4 content leads to a decrease in response of the composites. It is mainly due to the decrease of gas-sensing sites on the surface of $ZnFe_2O_4$ caused by the excessive coverage of g-C_3N_4 [43]. Besides, Fig. 5b shows the relation curve between operating temperature and response to 100 ppm acetone. All curves show a trend of first increasing and then decreasing at 119.3–230 °C [44].

Fig. 5c is the curves of the baseline resistance of the C_3N_4-$ZnFe_2O_4$ MSs and the pure $ZnFe_2O_4$ with the operating temperature. The resistance of the four sensors is negatively correlated with the operating temperature, which is consistent with the relationship between the resistance of the semiconductor and the temperature. Meanwhile, the resistance of four sensors follows an order of $ZnFe_2O_4$-30 (248 MΩ) > $ZnFe_2O_4$-20 (160 MΩ) > $ZnFe_2O_4$-10 (139 MΩ) > $ZnFe_2O_4$ (58 MΩ). As the amount of g-C_3N_4 modification increases, the resistance of the sensor rises, which may be attributed to the following factors. First, the potential barrier formed at the heterojunction interface and the electron depletion layer (EDL) on the g-C_3N_4 side play a negative role in the transport of electrons, as shown in Fig. 7b. In addition, the grain boundary barrier between g-C_3N_4 is also abundantly present in the composite. When the crystal grains are in contact with each other, the formation of the potential barrier will control the resistance of the material, thus causing g-C_3N_4-$ZnFe_2O_4$ MSs to exhibit a high resistance state.

The 3D histogram in Fig. 5d shows the response of pure $ZnFe_2O_4$ and

C_3N_4 modified $ZnFe_2O_4$ microsphere to 100 ppm gases at 161 °C. The $ZnFe_2O_4$-20 sensor has a higher response to acetone while a relatively low response towards ethanol, xylene, toluene, formaldehyde and benzene. However, pure $ZnFe_2O_4$ sensor has no obvious selectivity to a specific gas. The possible mechanism of selective enhancement could be explained as follows. First, the electron accumulation layer on the interface of the composite material promotes the chemical adsorption of oxygen [45]. Second, the g-C_3N_4 nanosheets on the surface of $ZnFe_2O_4$ can be used as active sites for catalyzing carbonyl or dehydrogenation reactions [46].

Fig. 6a exhibits the dynamic resistance transient of the $ZnFe_2O_4$-20 sensor at the range of 0.5–100 ppm acetone at 161 °C. The curve shows an approximate rectangle, and the response increased with the increased acetone concentration. Therefore, the sensor showed good acetone-detecting characteristics. Fig. 6b displays the changing law of the response with the increase of acetone concentration. The $ZnFe_2O_4$-20 sensor shows a rapid growth trend in the range of 1–50 ppm. However, the response increases slowly at a high concentration (50–500 ppm). As the acetone concentration increases, more molecules can be absorbed on the material surface and react with oxygen, resulting in increased response. However, as the concentration increases further, the response of the sensor tends to be saturated because a balance between the types of oxygen re-adsorbed and consumed can be achieved. In addition, the response to the low acetone concentration (0.5–10 ppm) at 161 °C can be seen in the inset of Fig. 6b. The result shows that the increase in response is linear, indicating that the sensor has potential application prospects in gas quantitative measurement. After calculation, the noise (RMSD) of the sensor is 0.183. According to the International Union of Pure and Applied Chemistry (IUPAC) standard, when the signal-to-noise ratio is greater than 3, the signal is considered true. Thus, the theoretical limit of detection to acetone is calculated to be 0.255 ppm with a slope of 0.58 ppm^{-1} [47].

To study the repeatability and stability of the sensor, we measure the dynamic acetone response and cycle performance. It can be seen from Fig. 6c that after 50 consecutive tests, the response is almost constant, indicating that the sensor has good robustness. We also study the dynamic 5 cyclic sensing transients of the $ZnFe_2O_4$-20 sensor to 100 ppm acetone (the inset of Fig. 6c). The sensor shows good response and recovery characteristics and good repeatability. As shown in Fig. 6d, the resistance of the $ZnFe_2O_4$-10 composite (135 MΩ) is higher than that of $ZnFe_2O_4$ microspheres (59 MΩ). HRTEM and XRD results show the presence of g-C_3N_4 on the surface, which will form the n-n heterojunction, resulting in an increase in the resistance of the composite. The response/recovery time of the sensor based on $ZnFe_2O_4$-20 to 100 ppm acetone is 17/21 s, respectively, while that of sample $ZnFe_2O_4$ is 2/30 s

Table S1 (Supporting Information) lists the acetone-sensing properties reported in the literature. The $ZnFe_2O_4$-20 microspheres in this work show a higher response (53.3 to 100 ppm acetone) and good selectivity. Compared with the other sensors, $ZnFe_2O_4$-20 microspheres have a relatively high response at moderate working temperature, which makes our sensors more competitive. For example, Fan et al. report that the sensor based on Co_3O_4 nanoparticles exhibit a response of 7.7 to 50 ppm acetone at 200 °C [48]. Although the operating temperature is relatively low, the response still needs to be improved. The $W_{18}O_{49}/Ti_3C_2T_x$ Mxene nanocomposite reported by Sun et al. can detect 20 ppm of acetone at 300 °C with a response of 10.5, but the operating temperature is as high as 300 °C, which limits its application [49].

3.3. Gas-sensing mechanism

The sensitive processes of SMOs usually include the adsorption of gas molecules, the reaction between measured gas and absorbed oxygen, and the electron transfer in the sensing material [50]. When n-type $ZnFe_2O_4$ is in air, the oxygen on the $ZnFe_2O_4$ MSs are ionized into oxygen species as O^- at 161 °C by trapping electrons, thereby generating an electron depletion layer and lowering the conductivity of the sensor.
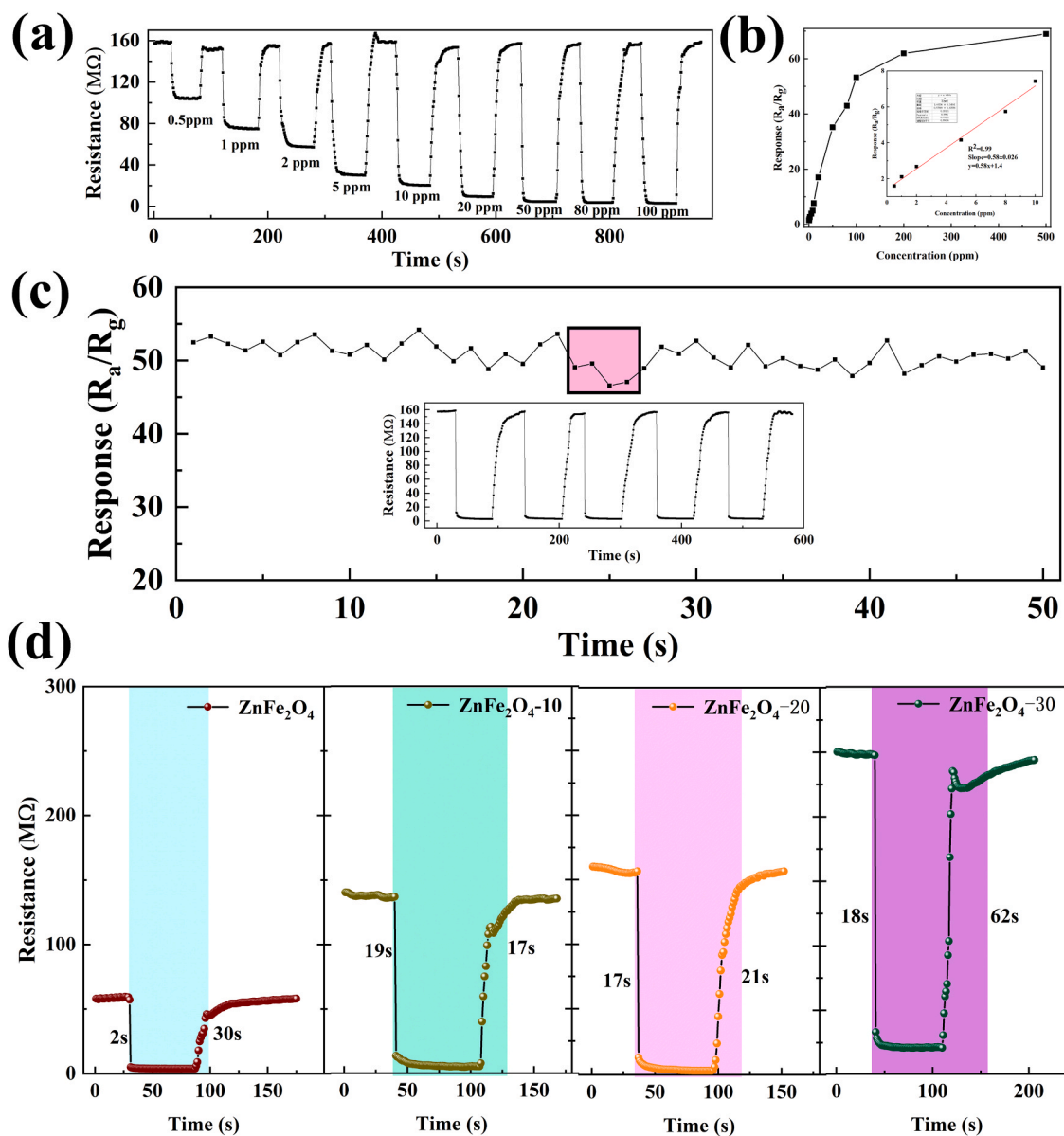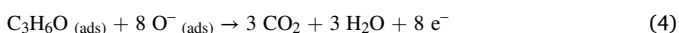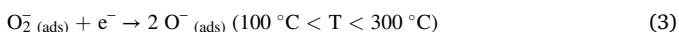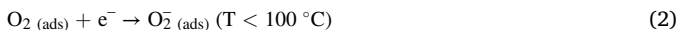
Fig. 6. (a) Dynamic gas sensing transients of ZnFe$_2$O$_4$-20 sensor to 0.5–100 ppm of acetone; (b) responses to acetone as a function of concentration at 161 °C and the inset in (b) show the response in the low concentration of acetone (0.5–500 ppm); (c) the response of ZnFe$_2$O$_4$-20 sensor to 100 ppm acetone at 161 °C versus cycle number and the inset in (c) show reproducibility of ZnFe$_2$O$_4$-20 on successive exposure to 100 ppm of acetone. (d) Dynamic resistance changes transients of the four sensors toward 100 ppm acetone at 161 °C.

Then, when the sensor is exposed to a reducing gas (acetone), the target gases will react with the adsorbed oxygen species and release electrons to the surface of the material, causing the sensor resistance to increase. The whole sensing process can be expressed as the following equations (Eqs. (1)–(4)) [3,51]:

$$O_2 \text{ (gas)} \rightarrow O_2 \text{ (ads)} \tag{1}$$

$$O_2 \text{ (ads)} + e^- \rightarrow O_2^- \text{ (ads)} \ (T < 100 \ °C) \tag{2}$$

$$O_2^- \text{ (ads)} + e^- \rightarrow 2 \ O^- \text{ (ads)} \ (100 \ °C < T < 300 \ °C) \tag{3}$$

$$C_3H_6O \text{ (ads)} + 8 \ O^- \text{ (ads)} \rightarrow 3 \ CO_2 + 3 \ H_2O + 8 \ e^- \tag{4}$$

Compared with pure ZnFe$_2$O$_4$ MSs, ZnFe$_2$O$_4$/g-C$_3$N$_4$ composites have better sensing performance, which could be caused by synergistic effects of the heterostructure, the catalysis of g-C$_3$N$_4$, and regulating the energy band structure. First, the heterojunction is the important factor to improve the response. According to the reported results, the conduction band (CB) edges of ZnFe$_2$O$_4$ and g-C$_3$N$_4$ are − 0.2 and − 1.28 V vs. NHE (Normal Hydrogen Electrode), respectively [52,53]. Combined with the bandgap value obtained by UV–vis test, the energy band diagram of ZnFe$_2$O$_4$ and g-C$_3$N$_4$ is shown in Fig. 7a. In the composite, due to the difference in work function (ZnFe$_2$O$_4$: 5.46 eV [54], g-C$_3$N$_4$: 4.21 eV [55]), electrons will transfer from g-C$_3$N$_4$ to ZnFe$_2$O$_4$ until the Fermi levels are equal, forming an electron depletion layer (EDL) and an electron accumulation layer (EAL) at the interface, respectively. Fig. 7b illustrates the energy band structure of the n-n heterojunction. It can be seen that the potential barrier established at the heterojunction and the EDL on the g-C$_3$N$_4$ side hinder the transfer of electrons on the composite, further leading to more obvious changes in the potential barrier and resistance before and after exposure to acetone. In addition, the HAL on the ZnFe$_2$O$_4$ side could make the electrons on the surface the important location for oxygen chemisorption [56], thus greatly promoting the acetone-sensing reaction on the surface of ZnFe$_2$O$_4$/g-C$_3$N$_4$.
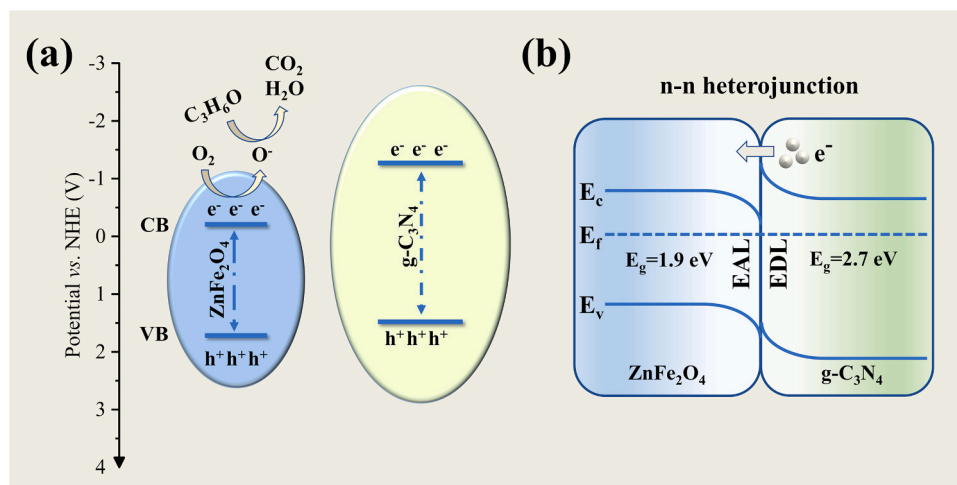
Fig. 7. Schematic energy band diagram illustrating the effect of g-C$_3$N$_4$ modification on acetone sensing.

Second, the g-C$_3$N$_4$ can also selectively catalyze the oxidation of methyl at a high temperature of 100–200 °C [47]. Third, according to the UV–vis DRS shown in Fig. 1b, the calculation results show that compared with unmodified ZnFe$_2$O$_4$, the bandgap of ZnFe$_2$O$_4$/g-C$_3$N$_4$ tends to increase (2.08–2.62 eV). Therefore, under the same conditions, the air baseline resistance (Ra) of g-C$_3$N$_4$-modified ZnFe$_2$O$_4$-based sensors is generally higher than that of pure ZnFe$_2$O$_4$-based sensors [57]. Subsequently, when the sensor is exposed to acetone, the ZnFe$_2$O$_4$/g-C$_3$N$_4$ sensor will have a higher resistance change, which will eventually lead to a higher response than pure ZnFe$_2$O$_4$.

4. Conclusions

In summary, we prepared the ZnFe$_2$O$_4$/g-C$_3$N$_4$ microspheres-based sensors with high sensitivity and selectivity for acetone detection. ZnFe$_2$O$_4$/g-C$_3$N$_4$ microspheres have a pleated structure composed of a large number of nanoparticles, which significantly provided abundant gas diffusion channels. Furthermore, the modification of g-C$_3$N$_4$ successfully increased the band gap of ZnFe$_2$O$_4$, thereby effectively optimizing the carrier concentration in ZnFe$_2$O$_4$ and increasing the baseline resistance of ZnFe$_2$O$_4$/g-C$_3$N$_4$ microspheres. The experiment results demonstrated that the ZnFe$_2$O$_4$-20 microspheres had good gas-sensitive properties to acetone, including good selectivity and linear response. The enhanced gas sensing properties could be ascribed to the catalysis of g-C$_3$N$_4$, regulating the energy structure, and heterojunction formation between ZnFe$_2$O$_4$ and g-C$_3$N$_4$. This work could not only provide a feasible route for the synthesis of ZnFe$_2$O$_4$/g-C$_3$N$_4$ microspheres but also prove that g-C$_3$N$_4$ modification is an effective strategy for the development of the ZnFe$_2$O$_4$-based functional materials, especially for gas detection.

CRediT authorship contribution statement

Wei Wang: Software, Writing – original draft. **Nan Zhang:** Conceptualization, Software. **Qilin Wang:** Formal analysis. **Xin Li:** Visualization, Investigation, Project administration. **Feng Li:** Methodology, Conceptualization, Formal analysis, Resources. **Shengping Ruan**: Supervision, Writing – review & editing, Validation, Funding acquisition.

Declaration of Competing Interest

The authors declare that they have no known competing financial interests or personal relationships that could have appeared to influence the work reported in this paper.

Acknowledgments

Appendix A. Supporting information

Supplementary data associated with this article can be found in the online version at doi:10.1016/j.jece.2023.111057.

References

[1] G.-J. Sun, H. Kheel, S. Park, S. Lee, S.E. Park, C. Lee, Synthesis of TiO$_2$ nanorods decorated with NiO nanopartieles and their acetone sensing properties, Ceram. Int. 42 (2016) 1063–1069.
[2] N. Zhang, S.P. Ruan, Y.Y. Yin, F. Li, S.P. Wen, Y. Chen, Self-sacrificial template-driven LaFeO$_3$/alpha-Fe$_2$O$_3$ porous nano-octahedrons for acetone sensing, ACS Appl. Nano Mater. 1 (2018) 4671–4681.
[3] Z. Lei, F. Dang, Y. Wang, S. Li, T. Wang, Y. Xu, et al., P-type hollow hexagram Co$_3$O$_4$ detect the acetone at low temperature and mechanism analysis, Chem. Eng. J. 471 (2023).
[4] H. Zhang, S. Guo, W. Zheng, H. Wang, H.-Y. Li, M.-H. Yu, et al., Facile engineering of metal-organic framework derived SnO$_2$-ZnO composite based gas sensor toward superior acetone sensing performance, Chem. Eng. J. 469 (2023).
[5] L. Fu, D. Li, W. Tang, High anti-humidity exhaled acetone sensor based on Co$_3$O$_4$ derived from MOF-74, J. Alloy. Compd. 960 (2023).
[6] D.J. Li, Y.L. Tang, D.Y. Ao, X. Xiang, S.Y. Wang, X.T. Zu, Ultra-highly sensitive and selective H$_2$S gas sensor based on CuO with sub-ppb detection limit, Int. J. Hydrog. Energy 44 (2019) 3985–3992.
[7] W.H. Tan, J.F. Tan, L.R. Fan, Z.T. Yu, J. Qian, X.T. Huang, Fe$_2$O$_3$-loaded NiO nanosheets for fast response/recovery and high response gas sensor, Sens. Actuators B-Chem. 256 (2018) 282–293.
[8] F.D. Qu, T. Thomas, B.X. Zhang, X.X. Zhou, S.D. Zhang, S.P. Ruan, et al., Self-sacrificing templated formation of Co$_3$O$_4$/ZnCo$_2$O$_4$ composite hollow nanostructures for highly sensitive detecting acetone vapor, Sens. Actuators B-Chem. 273 (2018) 1202–1210.
[9] W.T. Koo, S. Yu, S.J. Choi, J.S. Jang, J.Y. Cheong, I.D. Kim, Nanoscale PdO catalyst functionalized Co$_3$O$_4$ hollow nanocages using MOF templates for selective detection of acetone molecules in exhaled breath, ACS Appl. Mater. Interfaces 9 (2017) 8201–8210.
[10] S.D. Zhang, M.J. Yange, K.Y. Liang, A. Turak, B.X. Zhang, D. Meng, et al., An acetone gas sensor based on nanosized Pt-loaded Fe$_2$O$_3$ nanocubes, Sens. Actuators B-Chem. 290 (2019) 59–67.
[11] R. Zhang, T.T. Zhou, L.L. Wang, T. Zhang, Metal-organic frameworks-derived hierarchical Co$_3$O$_4$ structures as efficient sensing materials for acetone detection, ACS Appl. Mater. Interfaces 10 (2018) 9765–9773.
[12] X.Z. Song, F.F. Sun, S.T. Dai, X. Lin, K.M. Sun, X.F. Wang, Hollow NiFe$_2$O$_4$ microspindles derived from Ni/Fe bimetallic MOFs for highly sensitive acetone sensing at low operating temperatures, Inorg. Chem. Front. 5 (2018) 1107–1114.
[13] T.T. Zhou, T. Zhang, R. Zhang, Z. Lou, J.A. Deng, G.Y. Lu, et al., Constructing p-n heterostructures for efficient structure-driven ethanol sensing performance, Sens. Actuators B-Chem. 255 (2018) 745–753.

[14] F. Li, S.J. Guo, J.L. Shen, L. Shen, D.M. Sun, B. Wang, et al., Xylene gas sensor based on Au-loaded WO₃ center dot H₂O nanocubes with enhanced sensing performance, Sens. Actuators B-Chem. 238 (2017) 364–373.

[15] S.W. Choi, A. Katoch, J.H. Kim, S.S. Kim, Striking sensing improvement of n-type oxide nanowires by electronic sensitization based on work function difference, J. Mater. Chem. C. 3 (7) (2015) 1521.

[16] J. Hu, Y.H. Xie, X.F. Zhou, J.Y. Yang, Solid-state synthesis of ZnO and ZnFe₂O₄ to form p-n junction composite in the use of dye sensitized solar cells, J. Alloy. Compd. 676 (2016) 320–325.

[17] F. Zou, X.L. Hu, Z. Li, L. Qie, C.C. Hu, R. Zeng, et al., MOF-derived porous ZnO/ZnFe₂O₄/C octahedra with hollow interiors for high-rate lithium-ion batteries, Adv. Mater. 26 (2014) 6622–6628.

[18] J.H. Kim, J.H. Kim, J.W. Jang, J.Y. Kim, S.H. Choi, G. Magesh, et al., Awakening solar water-splitting activity of ZnFe₂O₄ nanorods by hybrid microwave annealing, Adv. Energy Mater. 5 (2015).

[19] X. Zhou, J.Y. Liu, C. Wang, P. Sun, X.L. Hu, X.W. Li, et al., Highly sensitive acetone gas sensor based on porous ZnFe₂O₄ nanospheres, Sens. Actuators B-Chem. 206 (2015) 577–583.

[20] L. Zou, H.R. Wang, G.L. Yuan, X. Wang, Magnetically separable CdS/ZnFe₂O₄ composites with highly efficient photocatalytic activity and photostability under visible light, ACS Appl. Nano Mater. 1 (2018) 831–838.

[21] R. Wang, L.N. Gu, J.J. Zhou, X.L. Liu, F. Teng, C.H. Li, et al., Quasi-polymeric metal-organic framework UiO-66/g-C₃N₄ heterojunctions for enhanced photocatalytic hydrogen evolution under visible light irradiation, Adv. Mater. Interfaces 2 (2015).

[22] F.D. Qu, S.D. Zhang, B.X. Zhang, X.X. Zhou, S.Y. Du, C.T. Lin, et al., Hierarchical Co₃O₄@NiMoO₄ core-shell nanowires for chemiresistive sensing of xylene vapor, Microchim. Acta 186 (2019).

[23] A. Argoub, R. Ghezini, C. Bachir, B. Boukoussa, A. Khelifa, A. Bengueddach, et al., Synthesis of MIL-101@g-C₃N₄ nanocomposite for enhanced adsorption capacity towards CO₂, J. Porous Mater. 25 (2018) 199–205.

[24] K. Wang, Q. Li, B.S. Liu, B. Cheng, W.K. Ho, J.G. Yu, Sulfur-doped g-C₃N₄ with enhanced photocatalytic CO₂-reduction performance, Appl. Catal. B-Environ., 176 (2015) 44–52.

[25] Y.F. Li, R.X. Jin, X. Fang, Y. Yang, M. Yang, X.C. Liu, et al., In situ loading of Ag₂WO₄ on ultrathin g-C₃N₄ nanosheets with highly enhanced photocatalytic performance, J. Hazard. Mater. 313 (2016) 219–228.

[26] J.Q. Wen, J. Xie, X.B. Chen, X. Li, A review on g-C₃N₄-based photocatalysts, Appl. Surf. Sci. 391 (2017) 72–123.

[27] C.S. Pan, J. Xu, Y.J. Wang, D. Li, Y.F. Zhu, Dramatic activity of C₃N₄/BiPO₄ photocatalyst with core/shell structure formed by self-assembly, Adv. Funct. Mater. 22 (2012) 1518–1524.

[28] F. Zhang, X.Y. Li, Q.D. Zhao, D.K. Zhang, Rational design of ZnFe₂O₄/In₂O₃ nanoheterostructures: efficient photocatalyst for gaseous 1,2-dichlorobenzene degradation and mechanistic insight, ACS Sustain. Chem. Eng. 4 (2016) 4554–4562.

[29] Z.W. Tong, D. Yang, T.X. Xiao, Y. Tian, Z.Y. Jiang, Biomimetic fabrication of g-C₃N₄/TiO₂ nanosheets with enhanced photocatalytic activity toward organic pollutant degradation, Chem. Eng. J. 260 (2015) 117–125.

[30] Y. Zeng, X. Zhan, B. Hong, Y. Xia, Y. Ding, T. Cai, et al., Surface atom rearrangement on carbon nitride for enhanced photocatalysis degradation of antibiotics under visible light, Chem. Eng. J. 452 (2022).

[31] Y.M. He, J. Cai, L.H. Zhang, X.X. Wang, H.J. Lin, B.T. Teng, et al., Comparing two new composite photocatalysts, t-LaVO₄/g-C₃N₄ and m-LaVO₄/g-C₃N₄, for their structures and performances, Ind. Eng. Chem. Res. 53 (2014) 5905–5915.

[32] F.A. Sofi, K. Majid, O. Mehraj, The visible light driven copper based metal-organic-framework heterojunction:HKUST-1@Ag-Ag₃PO₄ for plasmon enhanced visible light photocatalysis, J. Alloy. Compd. 737 (2018) 798–808.

[33] P. Niu, L.L. Zhang, G. Liu, H.M. Cheng, Graphene-like carbon nitride nanosheets for improved photocatalytic activities, Adv. Funct. Mater. 22 (2012) 4763–4770.

[34] J. Wang, W.D. Zhang, Modification of TiO₂ nanorod arrays by graphite-like C₃N₄ with high visible light photoelectrochemical activity, Electro Acta 71 (2012) 10–16.

[35] S. Kumar, T. Surendar, A. Baruah, V. Shanker, Synthesis of a novel and stable g-C₃N₄-Ag₃PO₄ hybrid nanocomposite photocatalyst and study of the photocatalytic activity under visible light irradiation, J. Mater. Chem. A 1 (2013) 5333–5340.

[36] M.J. Wang, Z.R. Shen, X.D. Zhao, F.P. Duanmu, H.J. Yu, H.M. Ji, Rational shape control of porous Co₃O₄ assemblies derived from MOF and their structural effects on n-butanol sensing, J. Hazard. Mater. 371 (2019) 352–361.

[37] Z. Wen, H. Ren, D. Li, X. Lu, S.W. Joo, J. Huang, A highly efficient acetone gas sensor based on 2D porous ZnFe₂O₄ nanosheets, Sens. Actuators B-Chem. 379 (2023).

[38] P. Li, C. Cao, Q. Shen, B. Bai, H. Jin, J. Yu, et al., Cr-doped NiO nanoparticles as selective and stable gas sensor for ppb-level detection of benzyl mercaptan, Sens. Actuators B-Chem. 339 (2021).

[39] W. Yao, Z.X. Xu, X. Xu, Y. Xie, W.J. Qiu, J.G. Xu, et al., Two-dimensional holey ZnFe₂O₄ nanosheetireduced graphene oxide hybrids by self-link of nanoparticles for high-rate lithium storage, Electro Acta 292 (2018) 390–398.

[40] Y.S. Fu, J.W. Zhu, C. Hu, X.D. Wu, X. Wang, Covalently coupled hybrid of graphitic carbon nitride with reduced graphene oxide as a superior performance lithium-ion battery anode, Nanoscale 6 (2014) 12555–12564.

[41] Y.S. Fu, T. Huang, B.Q. Jia, J.W. Zhu, X. Wang, Reduction of nitrophenols to aminophenols under concerted catalysis by Au/g-C₃N₄ contact system, Appl. Catal. B-Environ. 202 (2017) 430–437.

[42] X.Y. Chen, W.P. Wang, H. Xiao, C.L. Hong, F.X. Zhu, Y.L. Yao, et al., Accelerated TiO₂ photocatalytic degradation of Acid Orange 7 under visible light mediated by peroxymonosulfate, Chem. Eng. J. 193 (2012) 290–295.

[43] S. Bai, H. Liu, R. Luo, A. Chen, D. Li, SnO₂@Co₃O₄ p-n heterostructures fabricated by electrospinning and mechanism analysis enhanced acetone sensing, RSC Adv. 4 (2014) 62862–62868.

[44] N. Zhang, S.P. Ruan, J. Han, Y.Y. Yin, X. Li, C.X. Liu, et al., Oxygen vacancies dominated CuO@ZnFe₂O₄ yolk-shell microspheres for robust and selective detection of xylene, Sens. Actuators B-Chem. 295 (2019) 117–126.

[45] H.S. Woo, C. Na, I.D. Kim, J.H. Lee, Highly sensitive and selective trimethylamine sensor using one-dimensional ZnO-Cr₂O₃ hetero-nanostructures, Nanotechnology 23 (2012).

[46] L. Zhou, L.Z. Wang, J.L. Zhang, J.Y. Lei, Y.D. Liu, Well-Dispersed Fe₂O₃ Nanoparticles on g-C₃N₄ for Efficient and Stable Photo-Fenton Photocatalysis under Visible-Light Irradiation, Eur. J. Inorg. Chem. (2016) 5387–5392.

[47] F.D. Qu, W.A. Shang, D.T. Wang, S.Y. Du, T. Thomas, S.P. Ruan, et al., Coordination polymer-derived multishelled mixed Ni-Co oxide microspheres for robust and selective detection of xylene, ACS Appl. Mater. Interfaces 10 (2018) 15314–15321.

[48] X.X. Fan, Y.J. Xu, C.Y. Ma, W.M. He, In-situ growth of Co₃O₄ nanoparticles based on electrospray for an acetone gas sensor, J. Alloy. Compd. 854 (2021).

[49] S.B. Sun, M.W. Wang, X.T. Chang, Y.C. Jiang, D.Z. Zhang, D.S. Wang, et al., W₁₈O₄₉/Ti₃C₂Tₓ Mxene nanocomposites for highly sensitive acetone gas sensor with low detection limit, Sens. Actuators B-Chem. 304 (2020).

[50] D. Wang, K.C. Wan, M.L. Zhang, H.J. Li, P. Wang, X.Y. Wang, et al., Constructing hierarchical SnO₂ nanofiber/nanosheets for efficient formaldehyde detection, Sens. Actuators B-Chem. 283 (2019) 714–723.

[51] L. Lv, P. Cheng, Y. Zhang, Y. Zhang, Z. Lei, Y. Wang, et al., Ultra-high response acetone gas sensor based on ZnFe₂O₄ pleated hollow microspheres prepared by green NaCl template, Sens. Actuators B-Chem. 358 (2022).

[52] X. Guo, H. Zhu, Q. Li, Visible-light-driven photocatalytic properties of ZnO/ZnFe₂O₄ core/shell nanocable arrays, Appl. Catal. B-Environ., 160 (2014) 408–414.

[53] B. Zhang, X. Hu, E. Liu, J. Fan, Novel S-scheme 2D/2D BiOBr/g-C₃N₄ heterojunctions with enhanced photocatalytic activity, Chin. J. Catal. 42 (2021) 1519–1529.

[54] T. Yang, X. Yang, M. Zhu, H. Zhao, M. Zhang, Coral-like ZnFe₂O₄-ZnO mesoporous heterojunction architectures: synthesis and enhanced sensing properties for triethylamine, Inorg. Chem. Front. 7 (2020) 1918–1926.

[55] B. Zhu, L. Zhang, B. Cheng, Y. Yu, J. Yu, H₂O molecule adsorption on s-triazine-based g-C₃N₄, Chin. J. Catal. 42 (2021) 115–122.

[56] T. Wang, P. Sun, K. Chen, Y. Jiang, W. Tao, F. Liu, et al., MOF Structure engineering to synthesize core-shell heterostructures with controllable shell layer thickness: regulating gas selectivity and sensitivity, Sens. Actuators B-Chem. (2023) 378.

[57] T.S. Wang, I.C. Can, S.F. Zhang, J.M. He, P. Sun, F.M. Liu, et al., Self-assembly template driven 3D inverse opal microspheres functionalized with catalyst nanoparticles enabling a highly efficient chemical sensing platform, ACS Appl. Mater. Interfaces 10 (2018) 5835–5844.